Combustion and Emissions Study using a 7-point Lean Direct Injector Array

Focus on Flame Stability

Yolanda R. Hicks, Tyler G. Capil, Kathleen M. Tacina, and Robert C. Anderson
Yolanda.R.Hicks@nasa.gov
NASA Glenn Research Center
Engine Combustion Branch
Cleveland Ohio
United States of America

ABSTRACT

This paper continues a parametric study in which we consider the effect of air swirler configuration on the flame structure and combustor performance using a circular 7-point Lean Direct Injector Array for gas turbine applications. The injector array consists of a center swirler element surrounded by six swirler elements. Parameters considered in this study include swirler angle (60° or 52°), handedness (co-swirling or counter-swirling) and center swirler offset. The primary focus considers flame stability, comparing four key air swirler configurations: for 1) fuel-lean flames; 2) high cold flow air reference velocity flames. We determined that the baseline swirler configuration, consisting of all co-swirling 60° swirlers, had the best lean stability and could sustain the highest reference velocity. For this baseline configuration, we also compare the lean blowout limits of four reference fuels: three National Jet Fuels Combustion Program fuels—the A-2 "nominal" Jet-A, the C-1 two-component alcohol-to-jet (ATJ), and the C-4 ATJ/iso-paraffin blend—and the single component fuel n-dodecane. With regard to lean blowout, we determined that n-dodecane could sustain the leanest flame, followed by C-4 and A-2. C-1 was a poor performer.

Keywords: gas turbine combustors; fuel injection; fluid mixing

NOMENCLATURE

c	Center (swirler)
C_2*	Diatomic carbon radical
CH*	CH radical
CCW	Counter clockwise (swirl)
CRZ	Central Recirculation Zone
CW	Clockwise (swirl)
DCN	Derived Cetane Number
f	Focal length
f/	f-number, f-stop
FOM	Figures of Merit
LBO	Lean Blowout
LDI	Lean Direct Injection/Injector
LH	Left-Hand (swirl, swirlers)
M	Mach number
NBO	Near Lean Blowout
NJFCP	National Jet Fuels Combustion Program
NOx	Oxides of Nitrogen
o	Outer (swirlers(s))
P, p	pressure
PIV	Particle Image Velocimetry
RH	Right-Hand (swirl, swirlers)
SN	Swirl Number
T	temperature
U_{ref}	Cold flow reference velocity
UV	ultraviolet
V	velocity
3	Combustor inlet
4	Combustor exit

Symbols

ϕ	Equivalence ratio, fuel-to-air basis
x	Horizontal coordinate x
y	Horizontal coordinate y
z	Vertical coordinate z

1.0 INTRODUCTION

To minimize oxides of nitrogen (NOx) emissions from aircraft gas turbine combustors, NASA has advocated for fuel-lean strategies. That is, systems in which the fuel-air ratio stays predominantly lean throughout the combustor. Keeping the equivalence ratio, ϕ, well below the stoichiometric ratio keeps flame temperatures low, helping to minimize NOx production. Lower ϕ also supports low particulate matter (PM) emissions.

Over the last twenty or so years, NASA has explored a fuel lean strategy called lean direct injection (LDI), in which several smaller fuel injectors replace a traditional injector cup. The smaller LDI injectors help promote faster fuel-air mixing, leading optimally to a more uniform mixture. This uniformity reduces local hot spots to keep local instantaneous combustion temperatures as low as possible. LDI has demonstrated success in reducing NOx since inception during the High Speed Research (HSR) and Ultra-Efficient Engine Technology (UEET) Programs [1, 2]. The more recent NASA Programs, such as Fundamental Aeronautics, Environmentally Responsible Aviation,

and Advanced Air Transport Technology, have presented increasingly stringent challenges for NOx reduction. Using the initial design guidelines developed through parametric testing under HSR and UEET, LDI has met those challenges [3-7]. To continue to meet future emissions challenges as combustor conditions become more challenging, further design guidelines are needed. Supersonic cruise is a particularly challenging condition for combustor emissions.

There is currently renewed interest in flying commercial jets at supersonic speeds. To enable supersonic flight over land, NASA is leading a low boom flight demonstrator to investigate sonic boom noise mitigation [8-10]. Meanwhile, three companies, Aerion (2025, M1.4 Business Jet), Spike (2023, M1.6 Business Jet), and Boom (2023, M2.2 85-passenger airliner), have announced intentions to begin commercial flights as early as 2023 [11, 12] for either a business jet or small airliner. These latest efforts demonstrate the need to continue technology progress towards emissions reduction, particularly for NOx emissions. Engine cycles for supersonic cruise require a high inlet temperature, T3 and equivalence ratio, ϕ, resulting in a higher mean flame temperature at cruise; keeping the local instantaneous flame temperature low will be even more challenging than at the cruise condition for subsonic aircraft, increasing the importance of lean burn strategies.

Technical concerns for any lean burning system, including LDI, are increased susceptibility to lean blow out (LBO), flashback, and combustion dynamics compared to richer burning and staged rich-lean combustors [13]. The initial LDI design guidelines focused primarily on minimizing NOx emissions. Updated design guidelines will need also need to consider LBO, flashback, and combustion dynamics. In addition, these guidelines should be developed with alternative fuels in mind.

Alternative fuels are also being considered for both subsonic and supersonic aircraft as drop-in replacements or as mixtures with traditional refined fuels [14-15]. The National Jet Fuels Combustion Program (NJFCP) has been working to create a more expeditious and streamlined procedure for approving alternative jet fuels to be used by the aviation industry. Throughout the years, the NJFCP has established and tested a number of selected fuels to capture the effects and impacts that alternative jet fuels might have on significant operability limits called Figures of Merit (FOM). One of the FOM is lean blowout (LBO), which is the inlet condition for which a stable flame can sustain itself under the leanest possible fuel-air ratio before flame extinction. A number of LBO tests with different NJFCP fuels have been completed for bluff-body burners [16] and swirl-stabilized combustors [17] among others [18, 19]. These previous studies have shown a correlation between derived cetane number (DCN) and LBO limits where decreasing the DCN of a fuel resulted in LBO at higher equivalence ratios. In this paper we look to observe the effects of several types of conventional and alternative jet fuels on LBO for the current 7-point LDI hardware.

The subject 7-point LDI injector provides a low-pressure (5-atm) test bed to explore fuel-air mixing and the ensuing combustion. The 7-point LDI provides a way to determine the effects of air swirler angle and direction, and provides the option for a small amount of center swirler offset. In combination with the higher operating pressure 9-point injector (20 – 60-atm), and later generation LDI injectors, we are building a database to inform future design, and to provide reference data with which to anchor or compare models. In this paper, we will first present a brief overview of the results from the cold flow velocity measurements, which served to inform our decisions about the configurations which should be the focus of the combustion tests. We will then present the combustion test results with a focus on four primary configurations. The combustion test results include flame and chemiluminesce imaging from three key species: OH*, CH*, C_2*. We compare the flame structures based on these images. Finally, we present results with a focus on flame stability: we compare the fuel lean limit and the reference velocity limit for the chosen configurations; and we look at lean blowout limits for four reference fuels using the baseline swirler configuration.

2.0 HARDWARE AND EXPERIMENT

2.1 LDI Hardware

Figure 1 shows NASA LDI hardware used for practical study. The left side of figure 1 shows an end view of the 7-pt LDI hardware. The 9-pt array is depicted next. The 9-pt was a generation-1 design and was used extensively during HSR and is still used today for baseline testing of acoustics and for particulates measurement. The third configuration depicted is the 1-pt LDI. All three configurations use an injection element as described in the schematic drawing on the right. Each element is nominally 1-inch (25-mm) in diameter, and consists of an axial swirler, converging-diverging venturi and simplex atomizer. The simplex atomizer fits within the hub of the air swirler and its tip is positioned so that the fuel is injected at the venturi throat. The simplex nozzle produces a hollow cone spray with an angle nominally of 70°, and for the 1-pt and 7-pt, the flow number, FN_{US}, is 0.7. The air swirler has six-helical blades, with a hub diameter of 0.34-in (8-6-mm) outer diameter of approximately 0.875-inch (22.2-mm). The three swirler angles are 60° (baseline), 52°, and 45°. The calculated swirl numbers, as defined by Beer and Chigier [20] are 1.02, 0.77, and 0.59. The venturi throat diameter is 0.5-in (12.7-mm). The 7-pt and 1-pt have a venturi throat length of 0.061-in.

The elements of the 7-pt LDI are arranged with a center element surrounded by six equally-spaced elements on the outside in a hexagonal arrangement. The center-to-center spacing between adjacent nozzles (including the center element) is identical. Figure 2 shows details of the 7-pt hardware design, including swirler-venturi placement within the air box, through which all the inlet air flows.

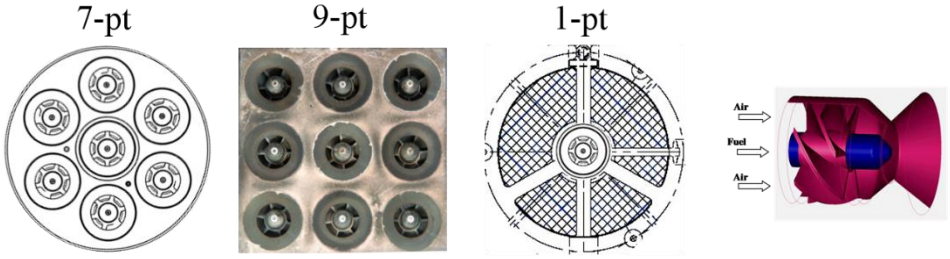

Figure 1 End views of the 7-pt LDI, the baseline 9-pt, and 1-point element arrangements. On right is an isometric drawing that shows the basic components of a single LDI element.

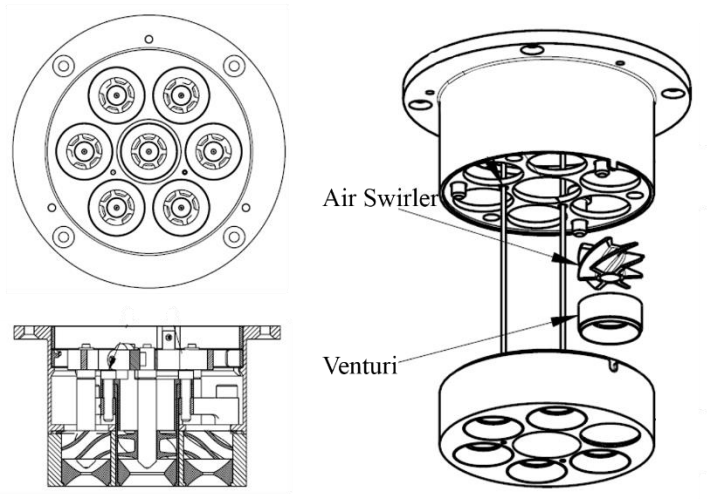

Figure 2 Details of the NASA 7-point LDI injector hardware and its assembly

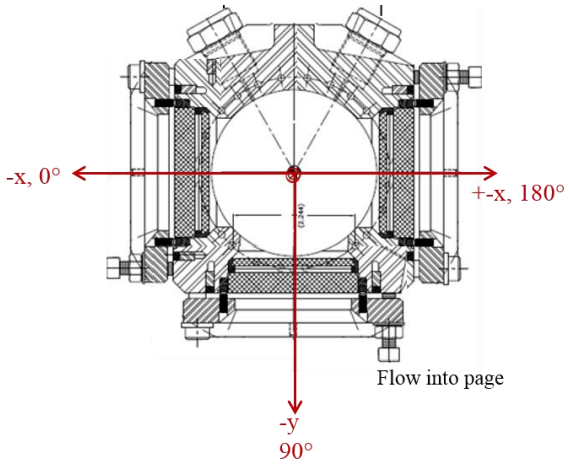

Figure 3 Schematic drawing that shows the plan view of the combustor

2.2 Test Facility

The facility used was the Combustion and Dynamics Facility (CDF), in which the flow through the combustor passes from top to bottom. The CDF can supply non-vitiated air preheated up to 1000°F (810 K) at air flow rates up to 0.8-lb_m/s (0.35 kg/sec) and pressures up to 5-atm (517-kPa). Figure 3 shows a plan view of the combustor section. The combustor test section is 15-cm long and has a circular cross-section nominally 7.62-cm in diameter (including the ceramic flame spray coating on the inner circumference). Three sets of double-paned windows, spaced 90° apart around its circumference, provide optical access to the water-cooled combustor. The windows are flat and have a small offset away from the combustor circumference. The windows measure 2.4-inch (6.1-cm) tall (axial direction) by 2.3-inch (5.8-cm) wide (azimuthal). Before the combustion products are exhausted, they are cooled using water spray. The first spray nozzle is approximately 10.5-in (26.7-cm) downstream of the combustor dome.

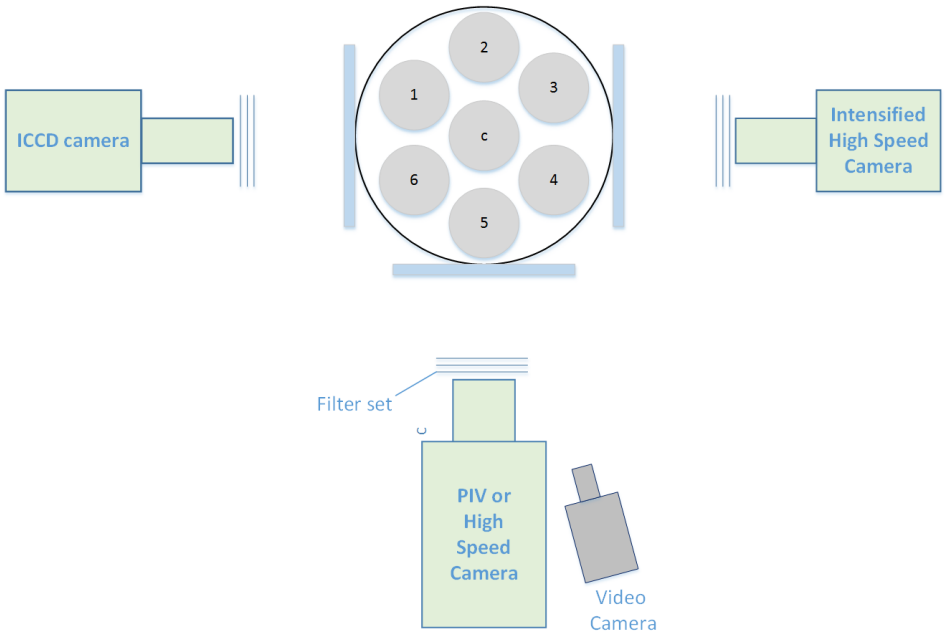

Figure 4 Imaging instrumentation layout plan view

2.3 Instrumentation and Procedure

The optical measurements described here include 2D velocity using standard PIV during cold flow testing, and of flame chemiluminescence imaging during combustion tests. For both measurements, we used an imaging layout similar to that illustrated in figure 4.

2.3.1

When performing PIV on the 7-point LDI, a laser beam was formed into a light sheet using a set of cylindrical lenses. The sheet passed through the test section and aligned parallel with the flow direction. The camera was positioned normal to the laser sheet and collected the light scattered by water droplets. The PIV data were acquired using a 15-Hz dual-head, frequency-doubled, Nd:YAG laser and a single, interline transfer, CCD camera. We traversed across the flow in 1-mm increments (generally from y = -24 to y = +24), and collected 500 image pairs per position. DaVis version 8.3 and PTU versions 9 and 10 (LaVision, Inc.) were used to collect to the PIV images. Data were collected at 5-bar, and 700K. Common cold flow reference velocities used for all cold flow tests were 75 ft/s, (22.9-m/s) and 50 ft/s (15.2 m/s).

DaVis version 8.1.2 software was used to process the PIV data. The same multi-pass cross-correlation vector processing was used on all data sets. We pre-processed the images by subtracting a sliding background. The processed results are axial horizontal-axial (x-z) components of velocity at each y-position.

2.3.2

For the flame chemiluminescence measurements, we used three scientific cameras, one per window, each focused on its corresponding vertical centre plane. On the -x side (left in figure 3, we used a gated, 16-bit, 1k × 1k pixel array, ICCD camera having a Gen II Super-Blue-Slow-Gate intensifier. We refer to this camera as ICCD. ICCD frame rates were typically 30-Hz. On the opposite (+x) side, we used a high speed, 12-bit, CMOS camera, 1k x 1k, equipped with a UV-intensifier, referred to as HSI. For HSI, we used an image resolution of 896 x 848 pixels and frame rate of 8-kHz. Finally, on the -y side (bottom camera in the image), we used a similar high-speed camera, without an intensifier, referred to as HS. With the HS camera, we used an image resolution of 320 x 368 and a much higher frame rate of 40-kHz. Note that the camera integrated line-of-sight field-of-view for the HS camera is different from the HSI and ICCD cameras. The HS integrates the emissions from three rows of swirler elements: 2-3-2. The HSI and ICCD cameras have more complex and overlapping swirler fields: 1-2-1-2-1.

For each camera, we used a remotely controlled filter wheel that allows us to select a species-specific filter (FWHM of 10-nm, typical) to pass light for that particular species through the lens to the camera. The filters used for each camera, to capture OH*, CH*, and C_2* were centered at 315-nm, 430-nm, and 515-nm, respectively. For the ICCD and HSI cameras, a UV-grade, f = 105-mm, f/4.5, macro camera lens for used to collect the transmitted light. For the HS camera, we used an f = 50-mm, f/1.2 camera lens. In addition to species-specific filters, we used neutral density filters with HS camera and/or used shutter speeds faster than the frame rate, to prevent over-saturating the CMOS detector. When performing the lean blowout tests, using the ICCD and HS cameras, we collected images without a filter. We also used a colour video camera during the LBO tests. As shown in figure 4, the video camera was positioned at a small angle with respect to normal.

2.4 Swirler configurations tested

We report on five different swirler configurations (including both the LH and RH baseline 60° swirler variants) of the 7-pt array, listed in table 1.

Table 1
Descriptive designations of the 7-pt swirler configuration variations described

Designation	Center Swirler	Outer Swirlers
RH60all	RH 60°	RH 60°
LH60all	LH 60°	LH 60°
RH60c_RH52o	RH 60°	RH 52°
LH60c_RH52o	LH 60°	RH 52°
LH60coff_RH52o	LH 60	RH 52°

2.5 Test matrices

Our standard combusting test incorporated variations to examine the effect of equivalence ratio and of reference velocity, as indicated in tables 2 and 3. For LBO tests, we selected one inlet condition that represented an idle condition, then held the fuel flow constant while increasing the air flow rate.

3.0 RESULTS AND DISCUSSION

We will first present a brief overview of the results from the cold flow velocity measurements, which served to inform our decisions on which configurations should be the focus of the combusting tests. We next will present the combustion test results with a focus on four primary configurations. The combustion test results are based primarily on imaging of flame and emission and chemiluminesce from three key species: OH*, CH*, C_2*. We compare the flame structures based on these species. Finally, we present results with a focus on flame stability. We compare the fuel lean limit, and the reference velocity limit for the chosen configurations; and we look at lean blow out for four reference fuels using the baseline swirler configuration.

3.1 Past results overview

Figure 5 provides a synopsis of our single point LDI non-reacting (cold flow) studies using a single point LDI [21]. Those test results indicated that the 60° swirler produced a CRZ, while the 45° and 52° swirlers did not. Recirculation zone formation was consistent with our testing of a corresponding 9-point array, in which we saw a CRZ behind all nine 60° swirlers [22].

Two seeding methods were used during the single point LDI tests. In one method, oil was seeded into the inlet air stream. In the second method used, we flowed water through the fuel nozzle, generally matching the fuel volume flow rate that would normally be used during combustion tests. Both seeding methods provided the information we sought: whether a CRZ forms downstream from the swirler. The main differences to consider regarding the two seeding methods are that

- oil-seeded air follows the air, and is a more traditional scheme for obtaining axial velocity
- water seeding through the fuel nozzle provides a combination of droplet velocity near the dome and air (for droplets that are small enough to follow the air)

The seeding method of flowing water through the fuel nozzle became our default method for comparing configurations because

1. it is simpler to implement
2. we were not limited by the smoke point temperature for oil
3. we could keep the windows clean.

For the single point 45° swirler, we saw in the air-seeded case that the high-velocity core that passed through the swirler did not much expand radially outward as it progressed downstream. The water spray was confined by that core air flow. For the 60° air swirler case, we saw that a CRZ did form, for both air seeding and water seeding. From these data, we hypothesized there would be less interaction between adjacent elements in the 7-point for the 45° swirlers compared to using the 60° swirlers. We therefore conducted both non-combusting and combusting tests and confirmed that with a center 60° swirler surrounded by 45° swirlers, a CRZ developed downstream of the 60° swirler but not downstream of the 45° swirlers. The same was the case with 52° swirlers on the outside. However, combusting tests that used the 45° degree swirlers could not sustain a flame very well and had a tendency to blow out.

Having established that only the 60° swirlers produce a CRZ, and that burning with 45° outer swirlers in was least stable, we focused these recent studies on testing configurations using

- all 60° swirlers, co-swirling. This is the baseline, either LH60all or RH60all
- 52° swirlers in the outer positions
- counter-swirl, primarily with the center swirler reversed from the outer swirlers
- center swirler offset, nested slightly upstream of the dome exit

In the last ISABE report [23], our tests indicated that whenever there were 60° outer swirlers, these outer swirlers prevented a center swirler CRZ from forming. When running the 7-point array with all 60°swirlers, we initially did not see a CRZ behind the center swirler. The three LDI configurations use identical swirlers and the fuel nozzles have the same size envelope, but the chamber shape and swirler spacing is different.

The apparent lack of a CRZ behind the 7-point center swirler led us to consider the possibility that the spacing between elements is close enough that interactions between the swirlers tends to prevent a center swirler CRZ from forming. The main feature different from the 9-point is the center-to-center distance between adjacent elements. For the 9-point, the closest adjacent spacing is 1-inch for the perimeter swirler elements and 1.414-inches between the diagonals. For the 7-point array, the spacing is the same for all elements and the center-to-center distance is 0.981-inches.

However, we remained concerned about that result, and pursued other seeding methods to confirm our result. For our LH60all configuration, we introduced water seeding in nozzles just upstream of the 7-point injector and compared those results to tests using our traditional method of using the center fuel nozzle for water-seeding. Both methods produced the same result in that there was now a center swirler CRZ; however, when earlier we saw six outer CRZs, we now saw only three outer swirler CRZs. As testing continued, we noticed increasing damage to swirler blades, particularly to the trailing edge, likely caused by repeated insertion and removal because the swirlers fit tightly in the 7-point housing, and require tapping to remove them. This is especially problematic for the 60° swirlers because their blades have more surface area contact than have the 52° or 45° swirlers. Considering that small swirler blade changes can result in relatively large changes in downstream fluid interactions [24, 25], we made new 60° RH swirlers and repeated our PIV tests using both the upstream water seeding and the fuel nozzle seeding. Results from both seeding methods indicated that all swirlers produced a CRZ, but that the center swirler CRZ is small. These results for the newly manufactured swirlers are described in the following section.

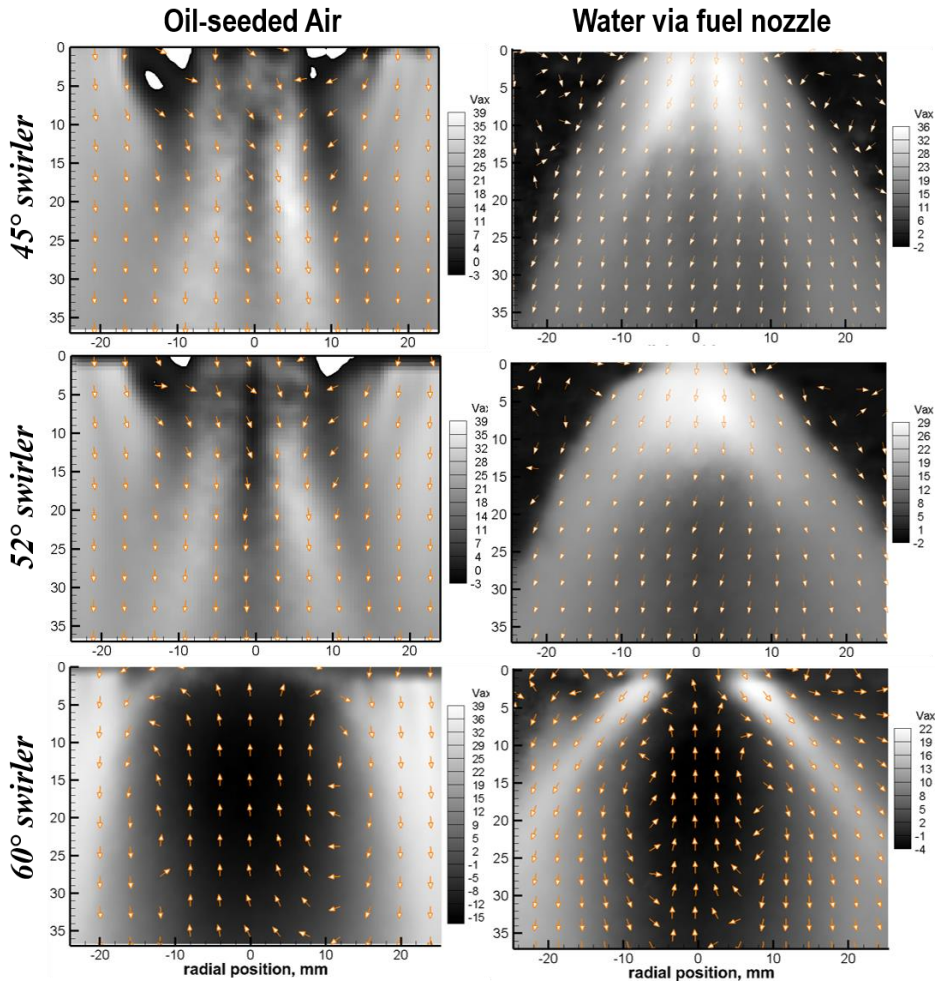

Figure 5 1-LDI results. Cold flow velocity with contour showing average axial velocity magnitude and vectors showing direction. Flow passes from top to bottom. Left column is oil-seeded air, with air flowing at uref = 50 ft/s, 45 psia, 300°F. Right column is water seeding through fuel nozzle with air conditions uref = 50 ft/s, 75 psia, 800°F. Areas near the dome for the 52° and 45° degree swirlers in the seeded air case are blanked (in white) to indicate locations of reverse flow

3.2 Cold flow results

Figure 6 shows results obtained during cold flow using PIV. The top row images present the axial velocity contours in the x-y plane at z ≅ 10-mm from the dome. The z = 10 axial velocity contours are individually scaled so that Vz < 0 is coloured in shades of blue. The bottom row images show the iso-velocity contours for Vz ≅ 0 obtained from the block of Vx-Vz images. Each iso-velocity contour is oriented to best observe the recirculation zone iso-surfaces. The four configurations (from left) are LH60c_RH52o, RH60c_RH52o, RH60coff_RH52o, and RH60all.

As we found with the single point and prior 7-point tests, only the 60° swirlers produce a CRZ. Correspondingly, only the RH60all configuration has a CRZ downstream of every swirler, although the center swirler CRZ volume and reverse velocity magnitude are very small in comparison to the outer swirler CRZs. For example, compared to the CRZ that appears most fully within the field of view (lower right in image), the center CRZ volume is roughly 2% of the CRZ volume of the outer swirler. It also has a smaller average velocity magnitude, about 6 times smaller. (These values appear on the Figure 7 graph as separate symbols.)

The relationship between CRZ size and velocity for these four configurations is plotted with connecting lines in figure 7, and arranged in order from largest to smallest center

CRZ volume. Of the configurations that have 52° swirlers, the co-swirling configuration, RH60c_RH52o, has the largest volume CRZ. In contrast, the counter-swirl configuration has the smallest volume, occupying about 10% of the volume of the co-swirling case. The center offset case is intermediate between those, and when one assumes the offset volume is primarily reverse flow, it is comparable—within 10% in volume (plotted as the open symbol in figure 7). The configuration with offset has a stronger CRZ in that its velocity is higher in magnitude than the non-offset configuration. Another distinction of the offset configuration is that it produces a CRZ that is compact and symmetric about the centerline, as compared to the configuration without any offset.

These results help confirm our observations that counter-swirl serves to isolate, but weaken the recirculation zone volume and velocity, and that a center offset also helps isolate the center swirler, but does not necessarily reduce the magnitude of reverse flow velocity.

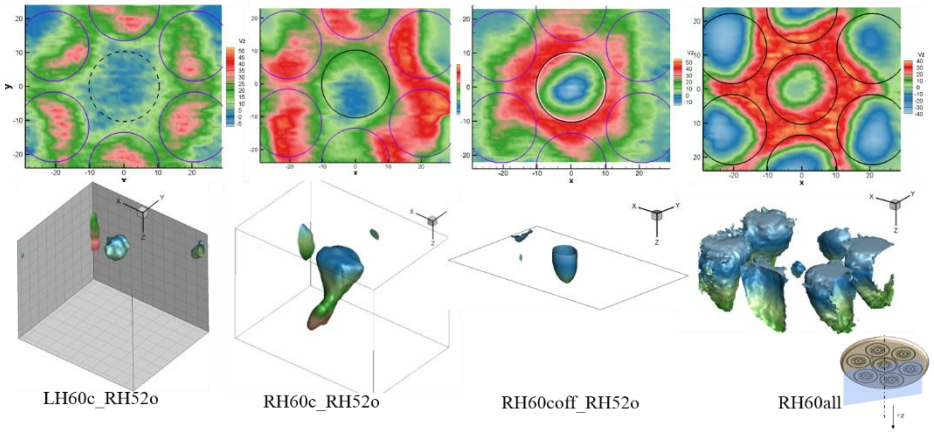

Figure 6 Cold flow PIV results for four 7-LDI swirler configurations. Top row: Contours of axial velocity at ~ z = 10-mm from dome. Bottom row: Iso-velocity contours of Vz = 0 that show the CRZ volumes, coloured by distance from dome

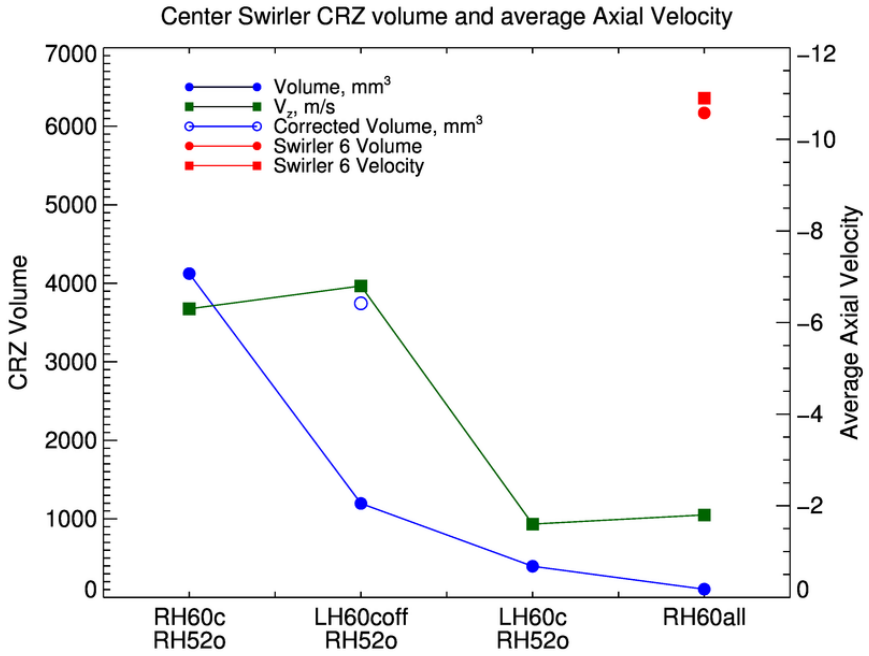

Figure 7 Chart showing the estimated CRZ volume (left y-axis) and axial velocity (right y-axis) for the swirler configurations shown on the x-axis

Table 2
Test matrix used to compare equivalence ratio effects

	ϕ overall	Fuel Flow/nozzle	
		lbm/h	kg/h
ϕ1	0.400	3.73	1.69
ϕ2	0.430	4.17	1.89
ϕ3	0.450	4.37	1.98
ϕ4	0.480	4.65	2.11
ϕ5	0.500	4.85	2.20

Table 3
Matrix used to consider reference velocity effects

	U_{ref}		Air flow		Fuel flow/nozzle	
	ft/s	m/s	lb_m/s	kg/s	lbm/h	kg/h
u1	30	9.1	0.237	0.107	3.73	1.69
u2	35	10.7	0.276	0.125	4.37	1.98
u3	40	12.2	0.316	0.143	4.98	2.26
u4	45	13.7	0.355	0.161	5.60	2.54
u5	50	15.2	0.394	0.179	6.22	2.82
u6	55	16.8	0.434	0.197	6.83	3.10
u7	60	18.3	0.473	0.215	7.36	3.34

3.3 Results of Combusting Tests

We tested each configuration at least twice. Each test consisted of a total rebuild of the injector configuration. Data from these repeats produced identical results with respect to operability, the fuel-lean limit, and maximum sustained reference velocity.

Tables 2 and 3 show the test matrices used to compare the configurations with respect to changes in equivalence ratio and to reference velocity, u_{ref}. The air inlet temperature and pressure were 800°F and 75-psia. For the tests that use these matrices, we assume all fuel nozzles are flowing the same quantity of fuel (even fueling). For the ϕ-matrix, u_{ref} is held fixed at 35-ft/s, and for the u_{ref} matrix, ϕ is held constant at 0.450. Because the outer swirlers are proximate to the windows, we limited the maximum equivalence ratio to 0.5 in order to ensure the un-cooled windows could maintain integrity over the course of the test. Despite this precaution, the inner window surface sometimes devitrified and became non-transparent, rendering the window unusable for optical diagnostics.

3.3.1 Overview—Flame structure revealed by OH* and CH* and C_2*

The intermediate combustion species OH*, CH*, and C_2* are considered to be indicators of the flame front location with OH* regarded as a good way to track relative combustion temperature [26, 27]. Indeed, we find that NO* is co-located with OH* [28, 29], and for fuel-lean systems NO formation is an exponential function of combustion temperature. Figures 8 and 9 show the average OH* structure that develops for each swirler configuration (column), and figure 10 shows the average CH* structure. Each image is an average of 7500 images acquired using the HSI camera during the final series of tests. The run order for these configurations is from left to right. Figure 11 shows CH* and C_2* images obtained using the high speed camera for configuration LH60coff_RH52o. Each figure has a cartoon image that shows a plan view of the camera perspective. For all images, flow passes from top to bottom.

Figures 8 – 10 show that each injector configuration results in a distinct flame structure. With respect to symmetry about the centerline (Y = 0), only the co-swirling configurations show symmetry over the entirety of both test matrices. Configuration LH60c_RH52o displays a clear asymmetry at all inlet conditions. The baseline configuration, LH60all is the thinnest and most uniform, and positioned closest to the dome. At the lowest two reference velocities, configuration LH60coff_RH52o has the most similar appearance to LH60all, but sets farther from the dome and is thicker. At the higher reference velocities, LH60all is the only configuration that does not present a distinct "pilot" region near the center swirler. LH60all is also the only configuration that has its signal minimum at the centerline, most likely because the center swirler CRZ is very small in comparison to the outer CRZs. For all configurations the OH*and CH* peak signals move downstream as the reference velocity increases.

3.3.2 Co-swirl vs counter-swirl

For the three configurations that have 52° outer swirlers, the co-swirling outer configuration, RH60c_RH52o produced the most symmetric field at all inlet conditions. This co-swirl configuration had three distinct zones that can be seen: first is the region immediately downstream of the center 60° swirler; the two remaining appear on either side of the centerline, and correspond to signal from the outer swirlers. The centerline symmetry becomes increasingly apparent with increasing u_{ref}. Also, as u_{ref} increases, the center zone signal increases and becomes comparable in intensity to the outer signal.

In comparison, the counter-swirl configuration shows a shift in outer zone signal—predominantly to the right side (+y) in these images. In addition, the shape downstream of the center swirler is different. In co-swirl the region appears flat and rectangular, but the counter-swirl the center region is near triangular, flat near the dome, with an apex downstream. This can best be seen at ϕ = 0.43 in figure 8, or the 45 ft/s images in figure 9.

3.3.3 CH* and C_2*

Figure 11 shows the CH* and C_2* image statistics—mean and RMS—for configuration LH60coff_RH52 at different reference velocities, obtained using the HS camera. The images are scaled independently. The HS camera images offer a different perspective from the HSI and ICCD cameras in that there are three rows of elements in the line-of-sight instead of five.

In comparing the CH* mean images from the HSI camera (figure 9, right column) with those from the HS camera mean (figure 11, left column), the trends are similar. At lower reference velocities, CH* persists farther downstream and has its highest signal in the center. The zone narrows and stays closer to the dome at higher reference velocities, and the signal tends to equalize between the center and outer elements.

In comparing C_2* with CH*, the overall trend is the same as noted above. The RMS images also removes some background noise to help emphasize the signal. For example, at the lowest reference velocity, it is clear that the downstream signal emanates from the outer swirlers, and we also note that C_2* persists a bit farther downstream at the 40-ft/s reference velocity. One key difference between C_2* and CH* becomes apparent at the higher reference velocities. Although both species show a trend for the signal from the outers to increase with reference velocity, for C_2*, the dominant signal is from the pilot region, whereas for CH*, the outer signal level grows to be on the order of the center region.

3.4 Flame stability

3.4.1 Regular matrix results

Figures 8 and 9 provide a simple illustration of performance with respect to flame stability. From most to least stable configuration for combustion, the order is LH60all, LH60coff_RH52o, RH60c_RH52o, and LH60c_RH52o. The most stable configuration was the LH60all because it could sustain the lowest equivalence ratio on the matrix (ϕ = 0.4) and also could sustain the highest reference velocity (60-ft/s). LH60all had a CRZ downstream of every swirler, which helped to support the flame. LH60coff_RH52o had a more isolated center, to act as a pilot; and when compared to its counterpart without the center recess (and poorest performer), could sustain an additional 10-ft/s reference velocity. RH60c_RH52o could sustain a reference velocity of 50-ft/s. If the offset effect is comparable, we would expect RH60coff_RH52 to match LH60all for reference velocity. As noted in the section on cold flow, we saw that a very distinct, moderately strong CRZ developed with that configuration.

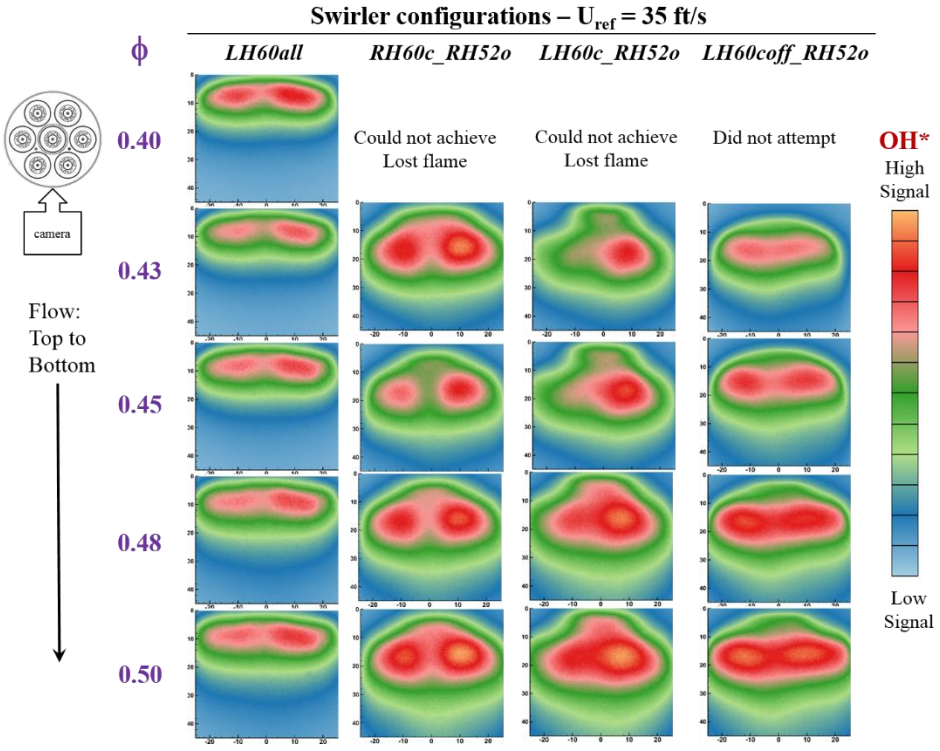

Figure 8 Images from HSI camera for four swirler configurations that reveal OH* structure for the equivalence ratios shown. Images within each configuration (column) are scaled together. Flow passes from top (nominally z = 0) to bottom. T3 = 800°F, P3 = 75-psia, u_{ref} = 35-ft/s

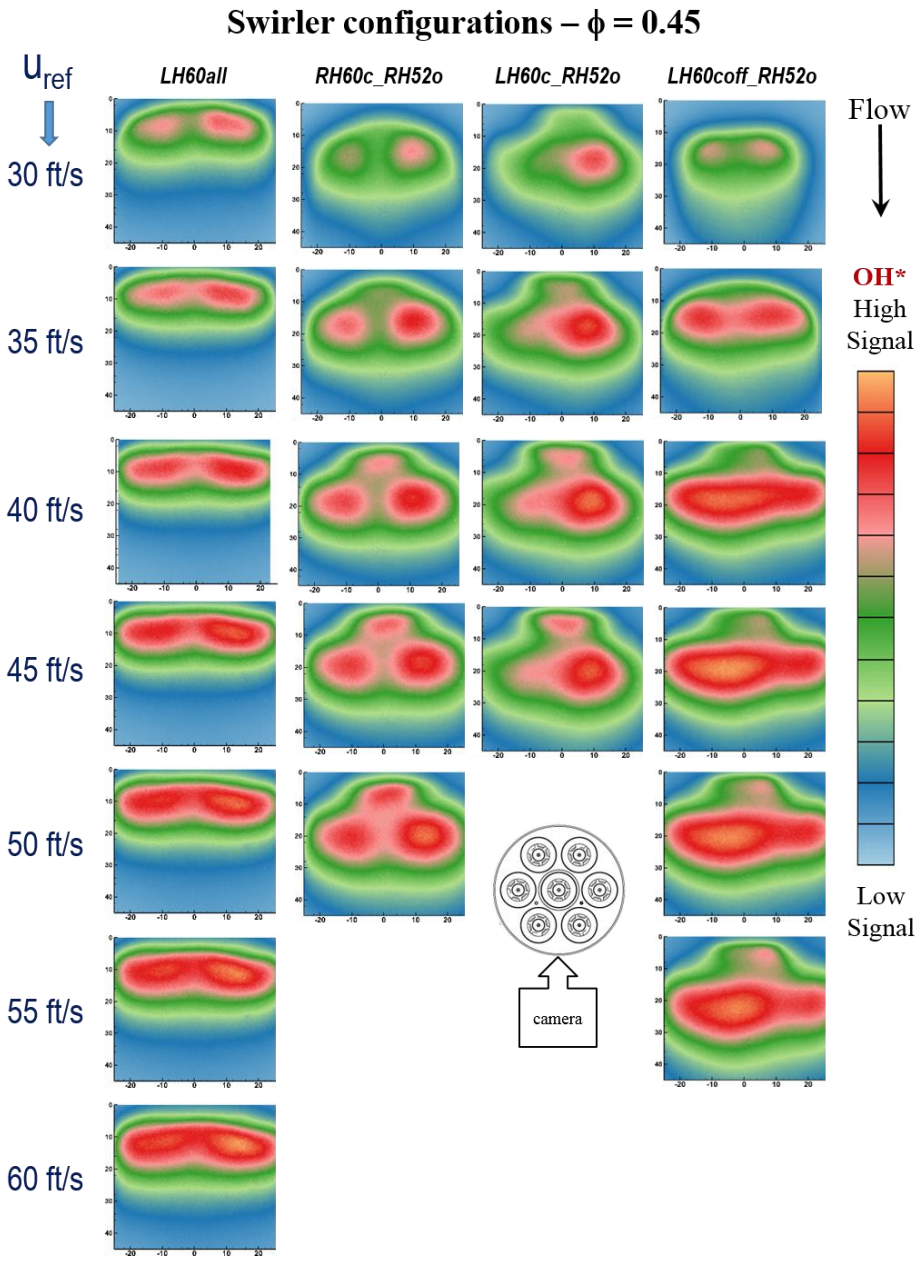

Figure 9 Images from HSI camera for four swirler configurations that reveal OH* structure for the reference velocities shown. Images within each configuration (column) are scaled together. Flow passes from top (nominally z = 0) to bottom. T3 = 800°F, P3 = 75-psi, ϕ = 0.45

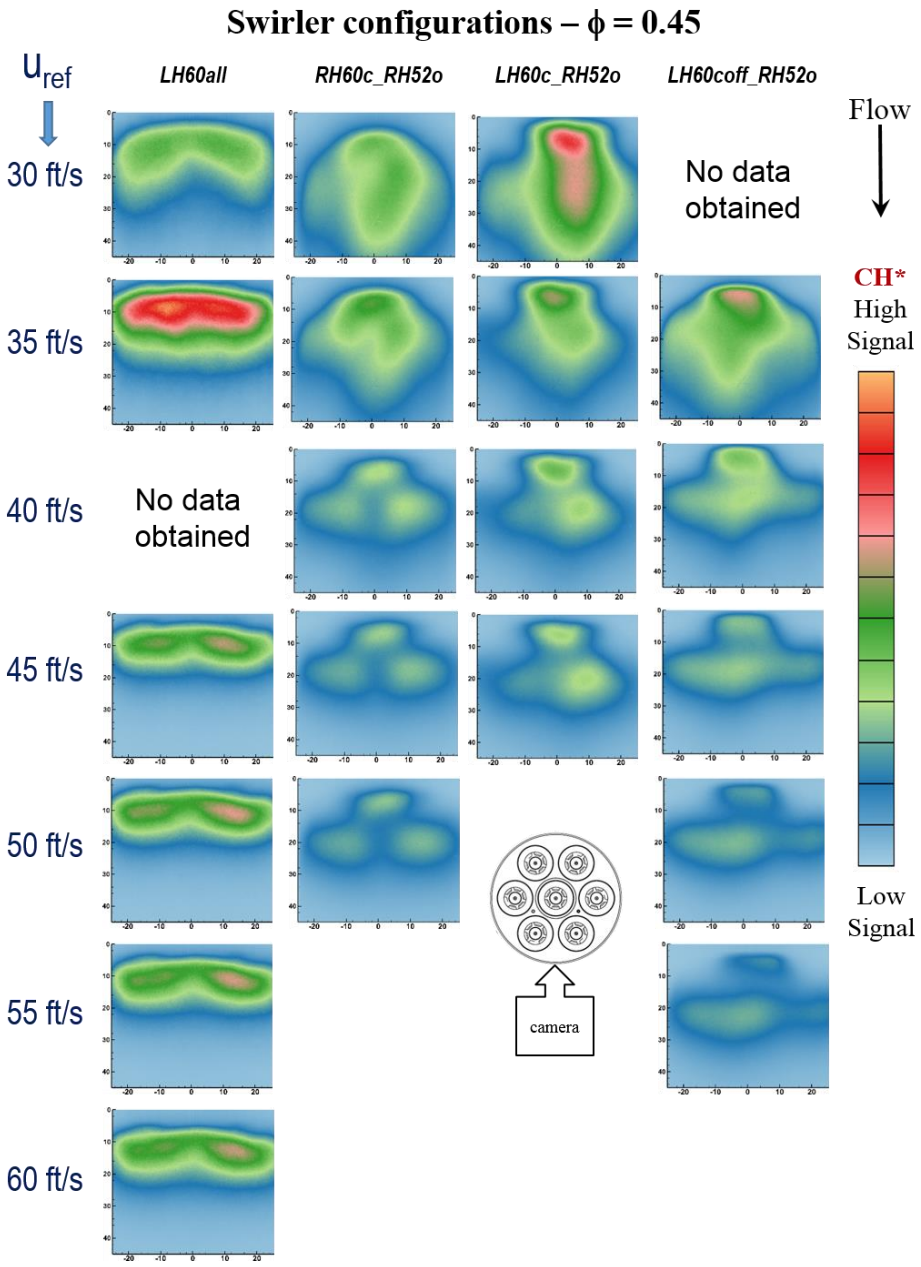

Figure 10 Images from HSI camera for four swirler configurations that reveal CH* structure for the reference velocities shown. Images within each configuration (column) are scaled together. Flow passes from top (nominally z = 0) to bottom. T3 = 800°F, P3 = 75-psi

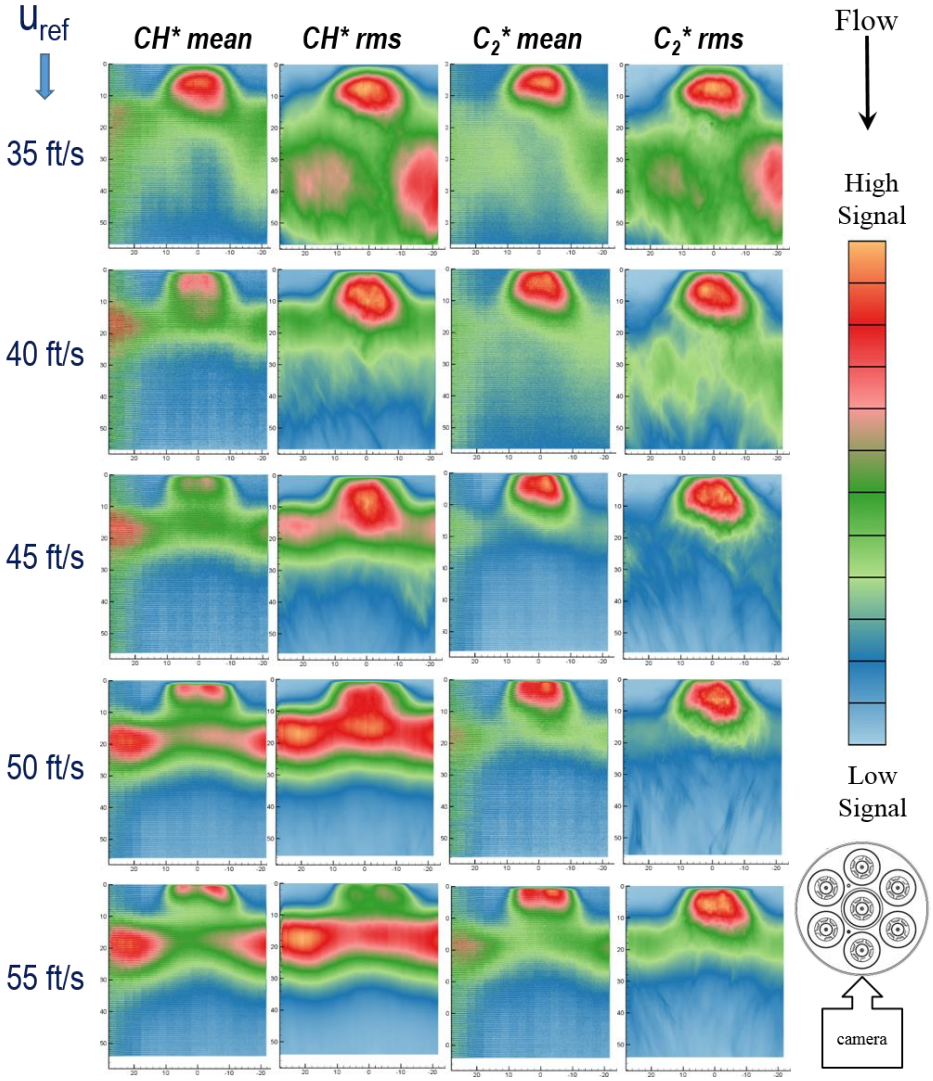

Figure 11 Images from HS camera for swirler configuration LH60coff_RH52o that reveal CH* and C_2* structure via mean and RMS for the reference velocities shown. Images are scaled individually. Flow passes from top (nominally z = 0) to bottom. T3 = 800°F, P3 = 75-psi

3.4.2 LBO

Lean Blowout (LBO) is another important consideration when evaluating overall fuel injector performance in a combustor. The National Jet Fuels Combustion Program (NJFCP) is using LBO as a Figure of Merit for evaluating and certifying alternative fuels. Most LBO tests have used conventional rich-front-end combustors. Additional data are needed for lean burn combustors, and the 7-point LDI combustor facility is a suitable venue for LBO testing. Using the baseline RH60all configuration, we evaluated LBO for three NJFCP reference fuels and one single component fuel.

The four fuels were chosen and tested to observe the effect of derived cetane number (DCN) on LBO. Table 4 provides a description and gives the composition of the four fuels. A-2 is a Jet A and represents a conventional-type jet fuel with average or nominal properties. The C-1, an alternative jet fuel, is a GEVO alcohol-to-jet (ATJ) composed of two iso-paraffins, C_{12} and C_{16}. C-1 has a notably low derived cetane number (DCN) of 16 compared to the DCN of 48 for Jet A. Because the C-1 fuel consists of only two components, the bimodal boiling range is unusual compared to typical jet fuels. The bimodal nature of C-1 has the potential to impact LBO in that one of the two components will vaporize before the other. As a result, this uneven vaporization can affect both fuel-air mixing and LBO. In order to achieve a wider, more conventional, boiling range while maintaining a low DCN of 28, C-4 fuel is used. C-4 is a blend

consisting of an iso-paraffinic kerosene (IPK) manufactured by Sasol (60%) with the balance being C-1 fuel. N-dodecane is neither a conventional-type nor alternative jet fuel for the NJFCP, but it provided a higher DCN (73.5) than the nominal A-2 fuel.

Table 4 Tested fuels for LBO. A comprehensive list of chemical and physical properties of the NJFCP reference fuels is detailed in [15, 30, 31]

Fuel	A-2	C-1	C-4	n-dodecane
POSF No.	10325	13572	12489	13226
Composition	Jet A	GEVO ATJ, highly branched C_{12} and C_{16} iso-paraffins	60% Sasol IPK (highly branched C_9-C_{13} iso-paraffins), 40% C-1	Straight chain C_{12} paraffin
Description	Average/ Nominal jet fuel	Very low cetane number with unusual boiling range	Low cetane number with conventional, wide-boiling range	High cetane number
DCN	49	16	28	73.5
Heat of combustion (MJ/kg)	43.1	43.9	43.8	44.5
Nominal formula	$C_{11.4}H_{22.1}$	$C_{12.6}H_{27.2}$	$C_{11.4}H_{24.8}$	$C_{12}H_{26}$
stoichiometric f/a	0.068026	0.066637	0.066536	0.066589

For each fuel, LBO was repeated 5-7 times. Although other facilities often performed many more repeats in order to develop good statistics for repeatability, we opted for a fewer number for three key reasons. First, the repeatability was excellent, with the standard deviation in ϕ at LBO only 2-6% of the mean and median values; see figure 12. Second, because as we approach LBO, the combustion efficiency decreases and the exhaust tends to become odorous, which disturbs our neighbours. Third, the windows become dirtier at the lower inlet temperatures, which prevents us from getting good optical data, but also may prevent us from lighting the combustor because we use our laser to ignite.

LBO testing was done at a low-power condition with only the center (pilot) fuel-air mixer fueled. To find the ϕ at LBO, the air mass flow rate is increased while holding the air temperature, air pressure, and fuel volume flow rate constant.

The steps in the LBO test sequence are as follows. After lighting off at our typical conditions, the flametube conditions were brought to the "near-LBO" conditions given in Table 5. The near-LBO conditions were held for several minutes while acquiring data for optical diagnostics images, combustion dynamics (pressure), test cell conditions, and gaseous emissions. Finally, the air flow rate was slowly increased until LBO occurred. During testing, LBO is observed visually. In post-processing, LBO is identified by a sudden drop in the gas temperature downstream of the combustor.

Table 5 Near-LBO inlet condition parameters. Only the center pilot nozzle was used.

$\mathbf{P_3}$	70 psia
$\mathbf{T_3}$	450 F
$\mathbf{m_{air}}$	0.300 lbm/s
$\mathbf{Q_{fuel,\ nominal}}$	2.01 gal/hr
$\mathbf{\Phi_{pilot}}$	1.275
$\mathbf{\Phi_{overall}}$	0.18

Figures 12 and 13 show the repeatability of both the near-LBO point and LBO. Figure 12 shows averaged chemiluminescence images for all five repeats of the near-LBO point for the C-4 fuel. The rows represent the nth time that the near-LBO condition was reached, and the columns represent the three chemiluminescent species that were captured: OH*, CH*, and C_2*. Comparing the rows within a single column shows the same qualitative flame structure over the five runs with very subtle differences. This repeatable flame structure provides confidence in the established starting condition before LBO was approached. Figure 13 uses a box-and-whiskers plot to show the distribution of ϕ at LBO for each of the four fuels. For each fuel, LBO is shown to be repeatable.

Figure 14 compares the flame structure of the near-LBO point for all four fuels. For all four fuels, the overall flame structure is similar. As would be expected with all 60° swirlers, the flames are short. Some asymmetry is present: each image shows favourability towards the left side of the field of view. In regards to peak signal, OH* peaks toward the left side whereas the CH* and C_2* peak at a slightly more central position.

Despite the overall similarity, there are minor but noticeable differences between fuels. These differences are larger than the repeat-to-repeat differences for a given fuel, as can be seen by comparing figure 14 with figure 12. Interestingly, C_2* displayed the most differences between fuels. For example, compare the C_2* images for the A2 and C-1 fuels (right column, top two rows). For the A-2* fuel, C_2* peaked throughout the upstream portion of the flame zone, whereas for the C-1 fuel, C_2* appears bimodal, with a slight split through the peak near the center of the flame and does not persist as far downstream.

The median reference velocity and the median overall equivalence ratio at LBO for each fuel is plotted as a function of the fuel's DCN in figure 15. The DCN indicates a fuel's tendency to auto-ignite and is used a surrogate for chemical timescale in previous work [18]. As figure 15 shows, reference velocity increases monotonically with increasing DCN. This trend of reference velocity with DCN is consistent with results from previous studies [16].

Consistent with the reference velocity results, the fuel with the worst LBO performance was the C-1 fuel which has the lowest DCN. In this case, the flame blew out at the highest overall equivalence ratio of 0.145. The n-dodecane fuel had the best LBO performance, blowing out at the lowest overall equivalence ratio of 0.113. LBO for the A-2 fuel occurred at an overall equivalence ratio of 0.130, which lies between C-1 and n-dodecane. This is expected based upon results from other groups [17, 19]. The C-4 fuel, which has a DCN between that of the A-2 and C-1 fuels, has typically shown an LBO equivalence ratio occurring between that of the A-2 and C-1 fuels. However, the results here differ in that the C-4 fuel performed better at LBO than A-2 by blowing out at a lower overall equivalence ratio of 0.126. There are many possible reasons for the disagreement, for example differences in spray quality due to differing viscosity, surface tension, and density. In addition, this LBO study had a key difference compared to most previous studies: LBO was found by increasing the air flow rate instead of decreasing the fuel flow rate. Therefore, we may need to assess the chemical timescale not only using cetane number but also the laminar burning velocity.

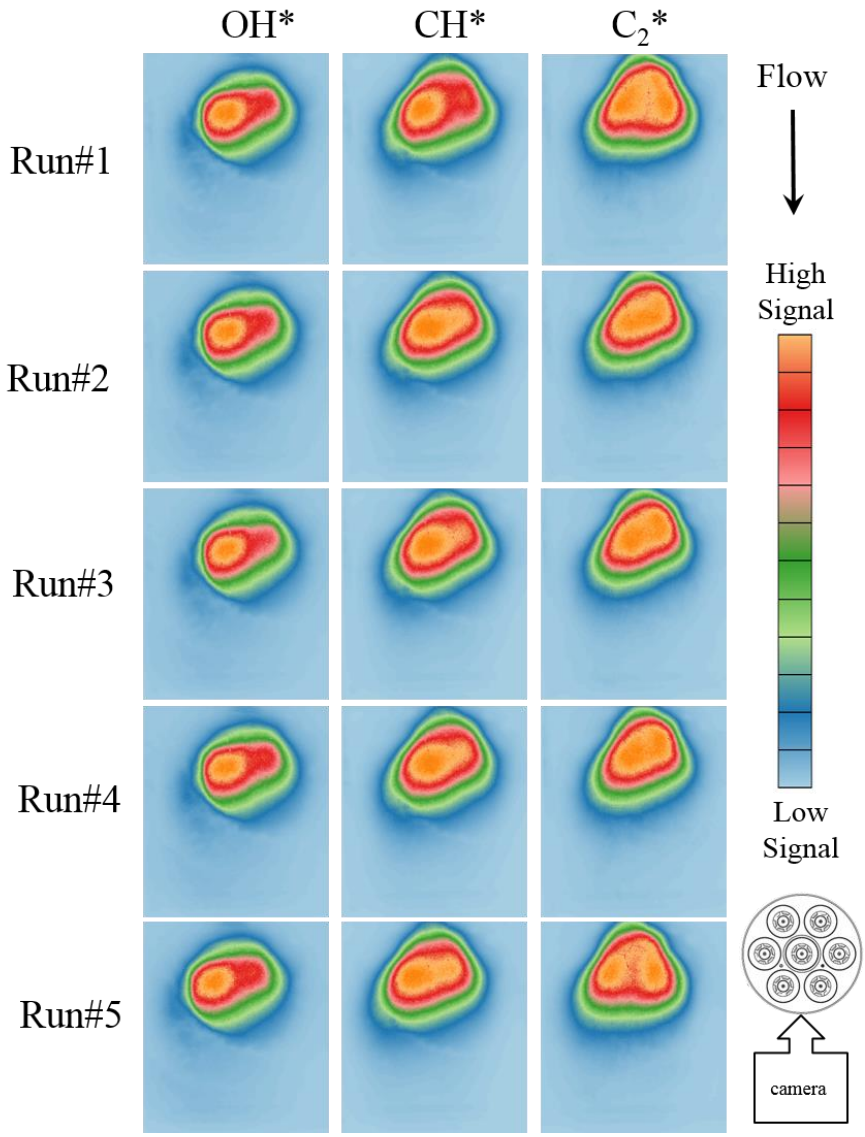

Figure 12 Images from the ICCD camera that reveal OH*, CH*, and C_2* for different runs of the NBO condition using C4 fuel. Swirler configuration RH60all

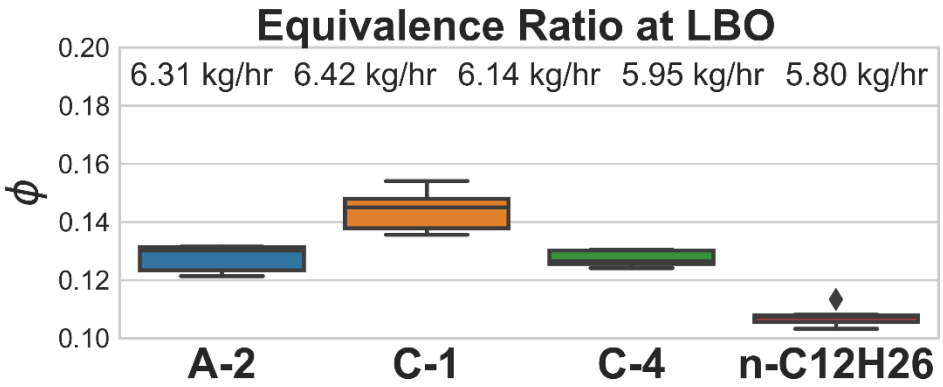

Figure 13 Box-whisker plots of the equivalence ratio at LBO for each fuel. Swirler configuration RH60all

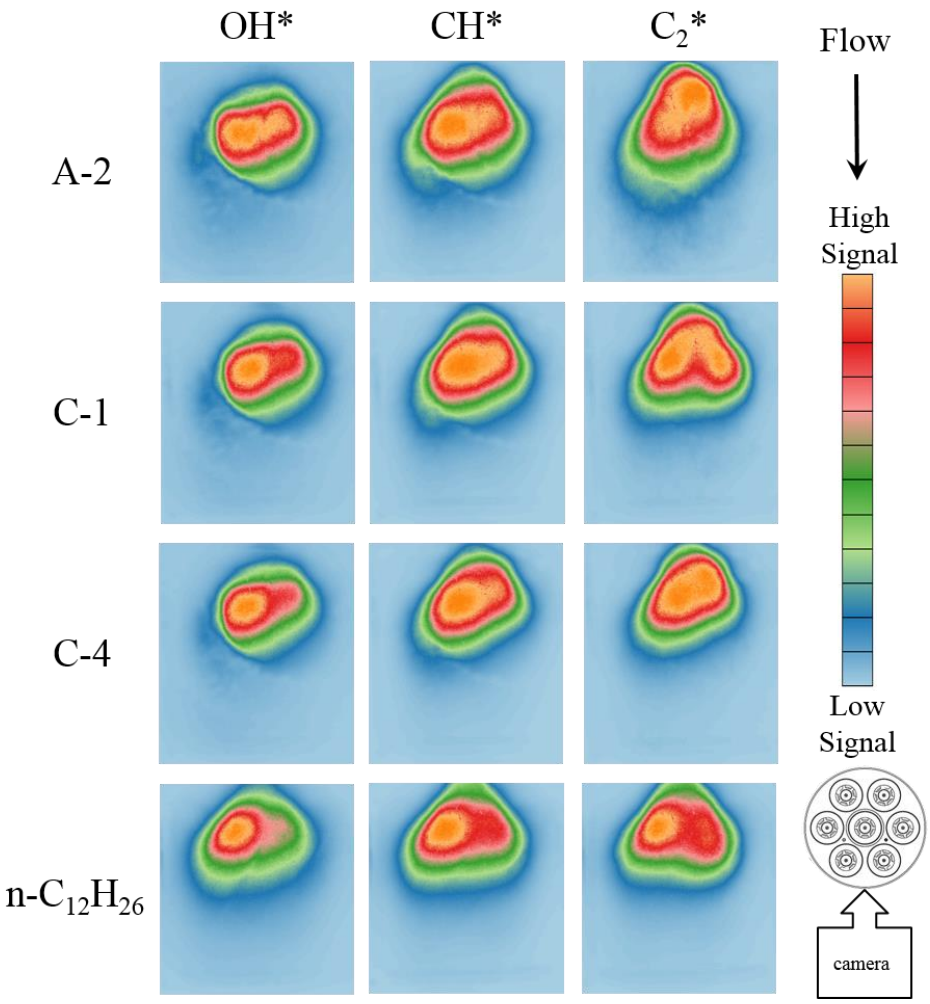

Figure 14 Images from the ICCD camera that reveal OH*, CH*, and C_2* for four different fuels at the NBO condition. Swirler configuration RH60all

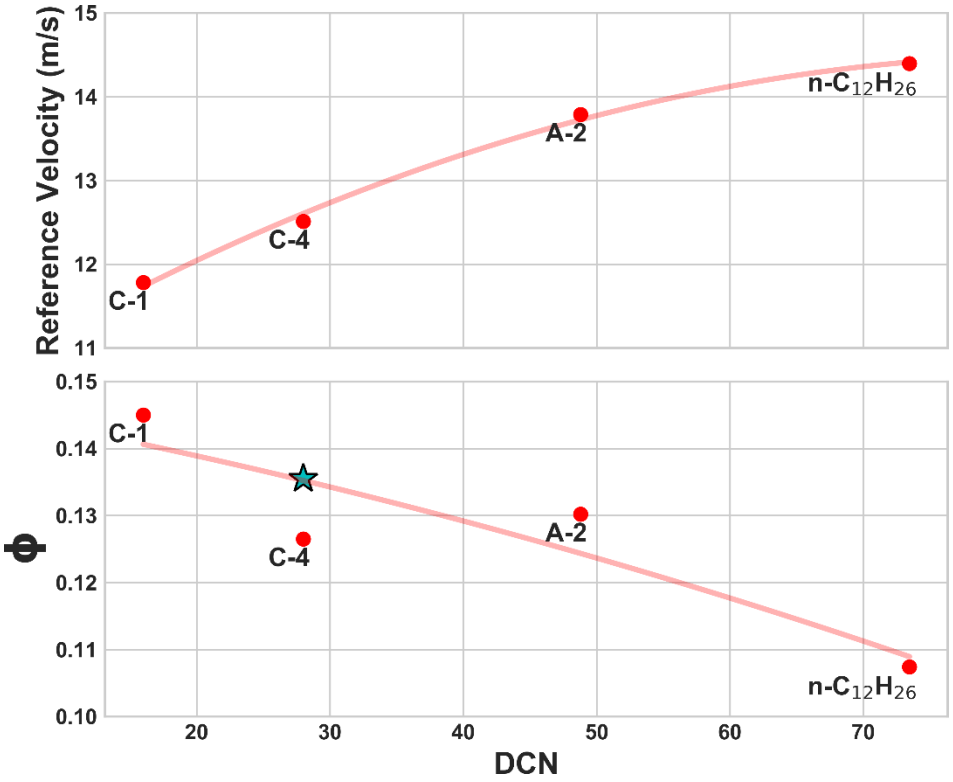

Figure 15 LBO results. Top: Reference velocity at LBO. Bottom: Overall equivalence ratio at LBO, both plotted as a function of DCN

4.0 SUMMARY

We presented results that complete the cold flow parametric survey of a 7-point LDI array, in which we considered the effects of air swirler angle, swirl direction and center swirler offset on the flow field immediately downstream from the dome and on the ensuing combustion. We noted that each swirler configuration resulted in a different flame structure, as observed using OH*, CH*, and C_2* species imaging.

We determined, by observing the fuel-lean limit and maximum reference velocity, which configurations could best sustain the flame. Based on these criteria, we determined that the baseline configuration, with all co-swirling 60° swirlers, had the widest operating range. With regard to lean blowout, we determined that n-dodecane fuel could sustain the leanest flame, followed by C-4 fuel and A-2 fuel. C-1 fuel was a poor performer.

Further work will include a deeper exploration of the speciation observed for the configurations studied, with a focus on flame chemistry.

ACKNOWLEDGMENTS

This work was supported by the Transformational Tools and Technologies Project under the NASA Aeronautics Research Mission Directorate.

REFERENCES

[1] R TACINA, P LEE, C WEY, "A lean-direct-injection combustor using a 9 point swirl-venturi fuel injector," ISABE-2005-1106, 2005.

[2] R TACINA, C WEY, P LAING, A MANSOUR, "A low NOx lean-direct injection, multipoint integrated module combustor concept for advanced aircraft gas turbines," NASA/TM—2002-211347, 2002.

[3] K AJMANI, P LEE, H MONGIA, "CFD computations of emissions for LDI-2 combustors with simplex and airblast injectors," Paper AIAA2014-3529, 2014.

[4] K M TACINA, C T CHANG, Z J HE, P LEE, B DAM, H MONGIA, "A Second Generation Swirl-Venturi Lean Direct Injection Concept," AIAA-2014-3434, 2014

[5] K M TACINA, D P PODBOY, Z J HE, P LEE, B DAM, H MONGIA, "A comparison of three second-generation swirl-venturi lean direct injection combustor concepts," Paper AIAA 2016-4891, 2016.

[6] K AJMANI, H C MONGIA, P Lee, "Parametric design of injectors for LDI-3 combustors," Paper AIAA 2015-3785, 2015.

[7] K M TACINA, D P PODBOY, B DAM, F P LEE, "A third-generation swirl-venturi lean direct injector combustor with a prefilming pilot injector," GT2019-90484, 2019.

[8] J MORGENSTERN, N NORSTRUD., J SOKHEY, S MARTENS, J J. ALONSO, "Advanced concept studies for supersonic commercial transports entering service in the 2018 to 2020 period, phase I final report," NASA/CR—2013-217820, 2013.

[9] K RAMAKRISHNAN ET AL., "Evaluation of low noise integration concpts and propulsion technologies for future supersonic civil transports", NASA/CR—2018-219936, 2018.

[10] J MORGENSTERN ET AL., "Advanced concept studies for supersonic commercial transports entering service in the 2018 - 2020 period, phase 2," NASA/CR—2015-218719, 2015.

[11] M MATOUSEK, "Aviation companies are plotting the return of supersonic flight - and they think their jets will be better than the Concorde," *Business Insider.com*, https://www.businessinsider.com/aviation-companies-are-plotting-the-return-of-supersonic-flight-2018-4, 29 April 2018.

[12] E ADAMS, "Even if you missed out on the Concorde, you may soon get a chance to fly in a supersonic airliner," *Popular Science*, https://www.popsci.com/supersonic-plane-next-generation/ 3 April 2019.

[13] T LIEUWEN, K MCMANUS, "Introduction: combustion dynamics in lean-premixed prevaporized (LPP) gas turbines," *Journal of Propulsion and Power*, Vol. 19, No.5, 2003.

[14] M COLKET ET AL, "An Overview of the National Jet Fuels Combustion Program", AIAA 2016-0177, 2016.

[15] T EDWARDS, "Reference jet fuels for combustion testing," AIAA 2017-0146, 2017.

[16] J A M SIDEY, P M ALLISON E MASTORAKOS, "The effect of fuel composition on swirling kerosene flames," Paper AIAA- 2017-0383, 2017.

[17] S D STOUFFER ET AL., "Lean blowout and ignition characteristics of conventional and surrogate fuels measured in a swirl stabilized combustor," Paper AIAA-2017-1954, 2017.

[18] E E PEIFFER, J S HEYNE, "Characteristic timescales for lean blowout of alternative jet fuels in four combustor rigs," Paper AIAA 2018-5914, 2018.

[19] R D STACHLER, J S HEYNE, S STOUFFER, J D MILLER, M ROQUEMORE, "Investigation of combustion emissions from conventional and alternative aviation fuels in a well-stirred reactor", Paper AIAA 2017-0382, 2017.

[20] J M BEER, N A CHIGIER, *Combustion Aerodynamics*, 1st ed., John Wiley & Sons, Inc., New York, 1972.

[21] S A TEDDER, K M TACINA, R C ANDERSON, Y R HICKS, "Fundamental study of a single point lean direct injector. Part I: effect of swirler angle and injector tip location". Paper AIAA 2014-3435, 2014.

[22] Y R HICKS, C M HEATH, R C ANDERSON, K M TACINA. "Investigations of a Combustor Using a 9-Point Swirl-Venturi Fuel Injector: Recent Experimental Results," Paper ISABE-2011-1106, NASA/TM-2012-217245, 2012.

[23] Y R HICKS, K M TACINA, AND R. C. ANDERSON, "Effect of Air Swirler Configuration on Lean Direct Injector Flow Structure and Combustion Performance with a 7-point Lean Direct Injector Array," Paper ISABE-2017-22620, 2017.

[24] J-F BOURGOUIN, J MOECK, D DUROX, T SCHULLER, S CANDEL, "Sensitivity of swirling flows to small changes in the swirler geometry," *Comptes Rendus Mecanique*, vol.341, pp. 211-219, 2013.

[25] J RUNYON ET AL., "Characterization or ALM swirl burner surface roughness and its effects on flame stability using high-speed diagnostics," GT2019-90215, 2019.

[26] J KOJIMA, Y IKEDA, T NAKAJIMA, "Basic aspets of OH(A), CH(A), and C2(d) chemiluminescence in the reaction zone of laminar methane-air premixed flames," *Combustion and Flame*, Vol. 140, pp. 34-45, 2005.

[27] V NORI, J SEITZMAN, "Evaluation of chemiluminescence as a combustion diagnostic under varying operating conditions," Paper AIAA 2008-953, 2008.

[28] Y R HICKS, T G CAPIL, R C ANDERSON, "Flame tube testing of a GEA TAPS injector: effects of fuel staging on combustor fuel spray patterns, flow structure, and speciation," Paper AIAA-2018-4476, NASA TM-2018-219984, 2018.

[29] Y R HICKS, R C ANDERSON, R J LOCKE, "Optical measurements in a combustor using a 9-point swirl-venturi fuel injector," Paper ISABE 2007-1280, 2007.

[30] J YANOWITZ, M A RATCLIFF, R L MCCORMICK, J D TAYLOR, M J MURPHY, "Compendium of experimental cetane numbers," NREL/TP-5400-61693, 2014.

[31] J H PERRY, C H CHILTON, S D KIRKPATRICK, editors, *Perry's Chemical Engineering Handbook*, 4th ed, McGraw-Hill, Inc., New York, 1963, p. 3-143.